ARTICLE   OPEN

Unexpectedly large energy variations from dopant interactions in ferroelectric HfO$_2$ from high-throughput ab initio calculations

Max Falkowski [1], Christopher Künneth [1], Robin Materlik [1] and Alfred Kersch [1]

Insight into the origin of process-related properties like small-scale inhomogeneities is key for material optimization. Here, we analyze DFT calculations of randomly doped HfO$_2$ structures with Si, La, and V$_O$ and relate them to the kind of production process. Total energies of the relevant ferroelectric Pbc2$_1$ phase are compared with the competing crystallographic phases under the influence of the arising local inhomogeneities in a coarse-grained approach. The interaction among dopants adds to the statistical effect from the random positioning of the dopants. In anneals after atomic layer or chemical solution deposition processes, which are short compared to ceramic process tempering, the large energy variations remain because the dopants do not diffuse. Since the energy difference is the criterion for the phase stability, the large variation suggests the possibility of nanoregions and diffuse phase transitions because these local doping effects may move the system over the paraelectric-ferroelectric phase boundary.

npj Computational Materials (2018) 4:73; https://doi.org/10.1038/s41524-018-0133-4

INTRODUCTION

Random distributions of the dopant positions may lead to variances of materials properties, causing unexpected but potentially useful effects. Distance-dependent interactions of dopants, as we demonstrate here on the example of La- and Si-doped HfO$_2$, lead to two different contributions in the variation of local energy density: (i) local variations of the concentration from random dopant positions, and (ii) local variations from dopant arrangement. An example of concentration variation is extrinsic channel doping in nanoscale transistors on the ppm level leading to a statistical variation of the small number of dopants in the device, measurable in the threshold voltage.[1] However, in ferroelectric materials like the newly discovered HfO$_2$ stabilized in the polar-orthorhombic phase,[2] doping concentrations are at least on the percent level because their mechanism is based on the modification of the local structure and free energy, affecting the phase stability.[3,4] For such large concentration c, one could expect a standard deviation $\sigma(\overline{E})$ of the mean energy density $\overline{E}$ resulting from $\sigma(\overline{c})$ and sensitivity as $\sigma(\overline{E}) = \frac{\partial \overline{E}}{\partial \overline{c}}\sigma(\overline{c})$, which is only significant for control volumes of small size L^3 containing few dopant atoms. However, we have found significant additional energy variations IQR(E) on the atomistic length scale ξ, resulting from the dopant−dopant interactions, which we calculate as $\xi \sim 1$ nm. They can be identified by choosing control volumes of edge size ξ in a coarse-grained approach to the free energy.[5,6] Furthermore, the doping concentration variation has the same interaction range; hence $L = \xi$, and the total energy variation results into the sum of $\sigma(\overline{E})$ and IQR(E)/2. Experimentally, especially in ferroelectric materials,[7] nanodomains of different doping concentrations may be found with different physical properties and diffusive phase transitions.[8–10] Positional static disorder has been proposed as the origin of relaxor ferroelectrics with exceptional piezoelectric and dielectric properties.[11,12]

Furthermore, nanolaminates have been processed and have shown improved ferroelectric properties in particular cases.[13–15] Although there is an enormous amount of experimental[16] and theoretical[17] work quantifying the influence of dopant order on average quantities, there is no theoretical work quantifying the local variation $\sigma(\overline{E}) + $ IQR(E)/2 that may occur on the scale ξ and relate them to the production process.

A very promising, recently discovered ferroelectric materials class is HfO$_2$ and ZrO$_2$,[2,18–21] which is based on the fluorite instead of the prominent perovskite structure.[22,23] The stabilization of the desired ferroelectric crystal phase is achieved with doping on the percent level.[24–27] Pure HfO$_2$ and ZrO$_2$ are chemically similar (i.e. they have a low atomic chemical potential[27]) and crystallize in the monoclinic P2$_1$/c phase (m-phase) at low temperatures. Under medium pressure (~10 GPa) a nonpolar, orthorhombic Pbca phase (o-phase) is stabilized. Differently, with increasing temperatures, the m-phase transforms first to the tetragonal P4$_2$/nmc (t-phase) and then to the cubic Fm$\overline{3}$m (c-phase) crystallographic phase. Appropriate doping concentrations can modify the materials characteristics of both HfO$_2$ and ZrO$_2$ for particular applications. For instance, by this means, the t-phase with a high dielectric constant $k \sim 40$ can be promoted to be the stable phase at room temperatures, utilized as insulator layers for metal-oxide-semiconductor field-effect transistors gates[28] and dynamic random access memory capacitors.[29] Another example is yttrium-doped ZrO$_2$ in the c-phase (YSZ), an important material for solid oxide fuel cells and gas sensors.[30] Finally, HfO$_2$ and ZrO$_2$ can exhibit ferroelectricity in thin films for certain doping concentrations.[4,18] The ferroelectricity arises from the polar, orthorhombic Pbc2$_1$ phase (p-o-phase).[31] Thus, HfO$_2$ and ZrO$_2$ are a lead-free and CMOS-compatible material class for applications like ferroelectric field-effect transistors, ferroelectric random access memory,[32] and pyro- and piezoelectric sensors.[4]

[1]Munich University of Applied Sciences, Lothstr. 34, 80335 Munich, Germany
Correspondence: Max Falkowski (max.falkowski@hm.edu) or Alfred Kersch (alfred.kersch@hm.edu)
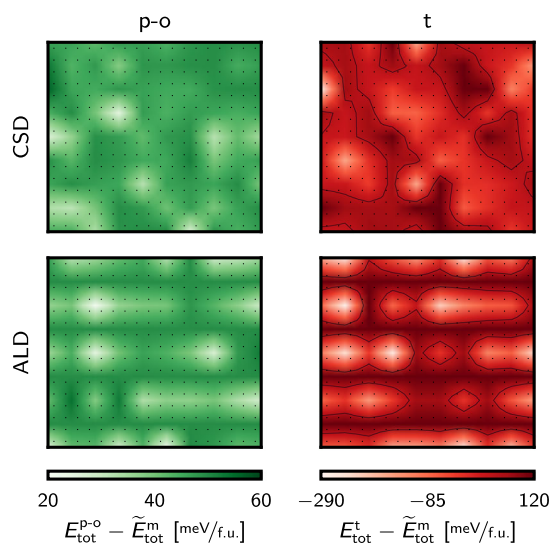
M. Falkowski et al.

Fig. 1 Energy landscapes of 9×10 nm^2 sections of Si-doped HfO$_2$ material in a coarse-grained approach with length scale $\xi = 1$ nm for the p-o-phase (left column) and the t-phase (right column). The CSD deposited material (upper row) is homogeneously doped with a concentration of 6.25 f.u.%. For the ALD deposited material (lower row), 1 nm layers of 12.5 f.u.% are followed by layers of 0 f.u.%. In the t-phase energy landscapes, the black contour lines indicate the boundary where the energy shifts locally below the energy of the p-o-phase

Crystal structures with dopants processed with a high thermal budget, such as ceramics, will approach their thermodynamic equilibrium configuration. In this lowest-energy configuration, the dopants are not necessarily randomly distributed but may develop a long-range order and the structural energy might be lower for such a distribution.[33] In contrast, the dopant distribution of chemical solution deposition (CSD)-manufactured films using a liquid precursor is believed to be almost random. After crystallization with a moderate thermal budget anneal,[19] local energy variations on the atomistic length scale from imprinted dopant positions remain. Yet another case are atomic layer deposition (ALD)-manufactured films. Since the host material (Hf or Zr) and the dopants are deposited in alternating layers, the doping distribution in the film deposition direction is enforced to follow the sequence of the layers whereas it is random in the layer plane. There are several experimental observations that require an explanation. The remanent polarization of ferroelectric Hf$_{0.5}$Zr$_{0.5}$O$_2$ ALD films,[34,35] which are actually nanolaminates depending on the cycle ratio of Hf and Zr, has been found to vary strongly with the laminate thickness ranging from 1 to 4 nm,[15] which can be considered as 1D nanoregion effects. The positions of dopants were investigated by Lomenzo et al.[36] and Richter et al.[37] They studied laminate structures from Si doping cycles in HfO$_2$ with the time-of-flight secondary ion mass spectrometry and high-resolution transmission electron microscopy (HR-TEM) after thermal processing and proved the limited mobility of cations in the low thermal budget ALD and CSD anneals. Oxygen, on the other hand, has been found to be very mobile,[38–40] allowing the formation or dissolution of dopant−oxygen vacancy defect configurations, depending on the oxygen supply and thermal processing. Finally, a temperature-induced polar to nonpolar phase transition in Si-doped HfO$_2$ has been found to be extremely broad.[41,42]

As pointed out in the last paragraph, each of the three processing techniques reveals different dopant distributions, which only in one case represents the thermodynamic equilibrium configuration with the lowest energy. Doping of HfO$_2$[25–27,43–45] and ZrO$_2$[46] was extensively researched utilizing the density functional theory (DFT) and using cluster expansion[30,33,47] or high-throughput calculations[48] under the premise that the lowest-energy structure is realized in thin films. Although all these studies attempt to answer the question of phase stabilization with doping, they do not consider the energy variation from the doping distribution enforced and biased by the processing technique. Attempting to fully cover the question of phase stabilization in HfO$_2$ from doping, the current study thoroughly investigates the influences of La and Si[37,49,50] doping (also considering oxygen vacancies), and their mixtures on the phases of HfO$_2$ for different doping concentrations and defect combinations, taking into account the dopant distribution of the different manufacturing processes. Since the goal is not to search for the lowest-energy incorporation of the dopant in HfO$_2$, the high-throughput approach is preferred to the cluster expansion. It is unavoidable to perform a numerous statistic of calculations for different arrangements of La and Si atoms in the HfO$_2$ matrix for a thorough study of the dopant mixture.

Some of the results can be condensed in a coarse-grained energy landscape (Fig. 1) which is fundamental for understanding local nanoregions that have been suggested in ferroelectric, doped HfO$_2$ based on HR-TEM observations.[51]

RESULTS

A first step in investigating the positional arrangements of defects and their combinations is to define the defects. As Künneth et al.[27] have shown that Si$_{Hf}$ and Si$_{Hf}$V$_O$ defects have similar impacts on the energetics in HfO$_2$, only the (i) Si$_{Hf}$ defect is considered in this study. On the contrary, La is a III-valent dopant in HfO$_2$ necessitating the consideration of oxygen vacancies (V$_O$). Following the work of Materlik et al.,[26] which computationally investigated La and V$_O$ defects in HfO$_2$ and showcased different DFT energies, we decided to focus on three La defects: (ii) electronically compensated La$_{Hf}$, (iii) mixed compensated La$_{Hf}$V$_O$ and (iv) ionically compensated La$_{Hf}$La$_{Hf}$V$_O$. Altogether, four defects are discussed in this study, which can be expressed using the Kröger-Vink notation as

(i) $1/2\mathrm{O}_2 + \mathrm{La}_2\mathrm{O}_3 \rightarrow 2\mathrm{La}'_{\mathrm{Hf}} + 4\mathrm{O}_\mathrm{O} + 2\mathrm{h}^{\cdot}$,

(ii) $\mathrm{La}_2\mathrm{O}_3 \rightarrow 2\mathrm{La}'_{\mathrm{Hf}} + 2\mathrm{O}_\mathrm{O} + 2\mathrm{V}^{\cdot\cdot}_\mathrm{O} + 2\mathrm{e}' + 1/2\mathrm{O}_2$,

(iii) $\mathrm{La}_2\mathrm{O}_3 \rightarrow 2\mathrm{La}'_{\mathrm{Hf}} + 3\mathrm{O}_\mathrm{O} + \mathrm{V}^{\cdot\cdot}_\mathrm{O}$ and

(iv) $\mathrm{SiO}_2 \rightarrow \mathrm{Si}_{\mathrm{Hf}} + 2\mathrm{O}_\mathrm{O}$.

Apart from the single defects defined in the previous list, selected defect pairs are investigated in this publication. Table 1 summarizes these defect combinations along with their supercell (SC) sizes, ensuring the defect concentration. Considering the symmetry of the different phases, the number of positional arrangements can be computed, which may be further reduced by thoughts detailed in the section "Geometries setup for the calculations" (# nonequiv.). A dash (−) separating two defects indicates that all positional arrangements of the defects pair are considered. For instance, in the case of the defect combination Si$_{Hf}$ − Si$_{Hf}$ all possible metal positions of the Si's in a 96-atomic supercell (992) are regarded. Conversely, defect constituents written in parentheses build a tightly packed defect. For instance, the combination (La$_{Hf}$V$_O$) means the V$_O$ is in the direct vicinity of the La$_{Hf}$ (next-neighbor). The selection of the defect combinations was generally performed with increasing complexity taking into account the computational effort of the DFT computations. Apart from the two simple defects, Si$_{Hf}$ and La$_{Hf}$, and their combinations, the mixed compensated (La$_{Hf}$V$_O$), the ionically compensated (La$_{Hf}$La$_{Hf}$V$_O$) and two complex defect pairs are considered in this study. Moreover, in the case of La$_{Hf}$ − La$_{Hf}$, Si$_{Hf}$ − La$_{Hf}$ and (La$_{Hf}$V$_O$), we considered two doping concentrations. For the remainder of this work, the collection of calculations of a certain supercell size and defect combination of all four crystal phases is referred to a

Table 1. Summary of the defect combinations, the supercell (SC) size, the resulting concentration for the four different phases in HfO_2

Defect combinations[a]	SC size[b]	Conc. [f.u.%]	Phase	# arrangements[c]	# nonequiv.[d]	Defect combinations[a]	SC size[b]	Conc. [f.u.%]	Phase	# arrangements[c]	# nonequiv.[d]
La_{Hf}	96	3.125	m	32	1	Si_{Hf}	96	3.125	m	32	1
			o	32	1				o	32	1
			p-o	32	1				p-o	32	1
			t	32	1				t	32	1
$La_{Hf} - La_{Hf}$	96	6.25	m	992	23	$Si_{Hf} - Si_{Hf}$	96	6.25	m	992	23
			o	992	23				o	992	23
			p-o	992	19				p-o	992 (864)	19 (16)
			t	992	9				t	992	9
$La_{Hf} - La_{Hf}$	48	12.5	m	720	34	$Si_{Hf} - La_{Hf}$	96	6.25	m	992	31
			o	480	25				o	992	31
			p-o	720	30				p-o	992	31
			t	720 (656)	12 (11)				t	992	9
$(La_{Hf}V_O)$	96	3.125	m	256	8	$Si_{Hf} - La_{Hf}$	48	12.5	m	720	45
			o	256	8				o	480	30
			p-o	256	8				p-o	720 (592)	45 (37)
			t	256	2				t	720	13
$(La_{Hf}V_O)$	48	6.25	m	384	24	$Si_{Hf} - (La_{Hf}V_O)$	96	6.25	m	7936	248
			o	256	16				o	7936	248
			p-o	384	24				p-o	7936	248
			t	384 (256)	4 (2)				t	7936	38
$(La_{Hf}La_{Hf}V_O)$	96	6.25	m	768	12	$Si_{Hf} - (La_{Hf}La_{Hf}V_O)$	96	9.375	m	23,040	360
			o	768	12				o	23,040	360
			p-o	768	12				p-o	23,040 (21,376)	360 (334)
			t	768	3				t	23,040	52

[a]Defect combinations in parentheses are positioned in vicinity (next-neighbors, tight defects)
[b]Nominal number of atoms in a supercell (SC) size. Introduction of an oxygen vacancy into the SC reduces the number of atoms by one. Nevertheless, the SCs with an oxygen vacancy are referred to as 48-atomic or 96-atomic
[c]Number of possible defect arrangements in the SC. Parentheses enclose the arrangements after filtering out the phase-transformed structures during the structural relaxation, as discussed in the section "Phase transformation detection during structural relaxation"
[d]Number of nonequivalent structures for which DFT calculations need to be performed. The reduction of needed calculations is discussed in the section "Geometries setup for the calculations". Parentheses enclose the number of structures that have stayed in the initial crystal phase during the structural relaxation

set. For instance, a set of pure HfO_2 calculations consists of four calculations, one for each crystal phase. Table 1 lists 12 sets of 12 different defects and concentrations.

In order to be able to compare different defect types containing different atom species, a unified concentration definition is needed. One formula unit (f.u.) is defined by one metal and two oxygen sites. For instance, a 96-atom supercell contains 32 f.u.s. Placing one La_{Hf} or $(La_{Hf}V_O)$ defect into the cell results in a concentration of 3.125 f.u.%, because both defects need exactly one of 32 f.u.s. Opposed to these defects, $(La_{Hf}La_{Hf}V_O)$ needs two f.u.s, resulting in a doubled concentration of 6.25 f.u.%.

The boxes in Fig. 2 show DFT energies of the four phases with respect to the energy median $\tilde{E}$ of the m-phase carried out for the defect combinations tabulated in Table 1. For instance, the box-plots for the 6.25 f.u.% $La_{Hf} - La_{Hf}$ defect in Fig. 2a represent in each case 992 $La_{Hf} - La_{Hf}$ different positional arrangements in the 96-atomic supercell, although only the symmetric nonequivalent arrangements as listed in Table 1 are computed with DFT. This was achieved by weighting the symmetric nonequivalent arrangements with their number of symmetry equivalent possibilities.

Experimental measurements on doped HfO_2 show that 3 f.u.% to 5 f.u.% Si-doped HfO_2[37] and 7−15 f.u.% La-doped HfO_2[49] is ferroelectric. However, even the defect arrangements with the lowest energy of the statistic (manufacturing processes with large thermal budget) in Fig. 2 alone cannot explain the stabilization of the p-o-phase, which is believed to be responsible for the ferroelectricity, over the o-phase and m-phase. As discussed in other studies[25–27,45,52–54] for several dopants, there are mechanisms to exclude the o-phase and m-phase in thin films and doping affects only the competition between t-phase and p-o-phase under these conditions. A more detailed discussion of these mechanisms for doped HfO_2 with La and Si can be found in the supplementary materials. It should be noted that for La and Si, an in-depth discussion of the phase stability was held in the publications of Materlik et al.[26] and Künneth et al.,[27] respectively, and the current study confirms their findings qualitatively.

DISCUSSION

As the calculated energy distributions are not Gaussian, we use median instead of mean quantities. Figure 3a–d illustrates the DFT energy medians of Fig. 2 of the four defects against their defect concentration which turn out to be almost linear, following the linear response rules. This linear response of La doping up to 12.5 f.u.% found here (Fig. 3a) with the statistical approach is in contrast to the nonlinearity of the DFT energies of the t-phase for 12.5 f.u.% defect concentration which was recently found by Materlik et al.[26] considering the lowest-energy structures
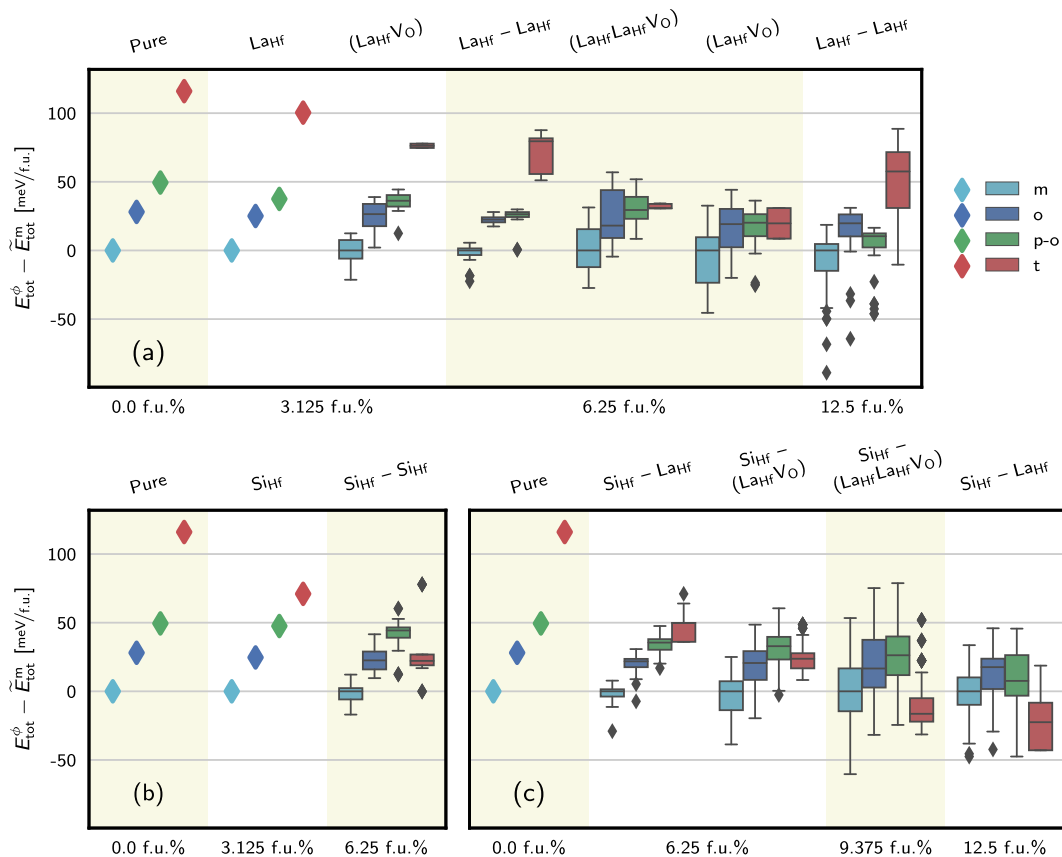
Fig. 2 The total energies of the La defects **a**, Si defects **b**, and their mixtures **c** in HfO_2. The big colored diamonds mark single data points. The box diagrams depict the distributions of data points: the colored box body marks the lower and upper quartiles, the line in the box is the median, the whiskers are the lowest and the highest values neglecting the outliers, which are marked by small black diamonds. The quartets of colored diamonds or box diagrams represent the *sets*, as described in Table 1. They are sorted in an ascending order of concentration along the horizontal axis. The background color associates the *sets* with defect concentration labels at the bottom edge and the defect type itself is labeled at the top edge. The four colors mark different crystal phases as described in the legend. All *sets* are referenced to the corresponding m-phase data point or distribution median $\tilde{E}_{tot}^{m}$

(see supplementary materials). With the statistical approach, the p-o-phase becomes bulk stable at 15.5 f.u.%, if extrapolated.

The energies of the $(La_{Hf}V_O)$ defect in Fig. 3b exhibit a slight nonlinearity in the DFT energies with the defect concentration, especially the o- and t-phases. Two possible explanations are conceivable: (i) the $(La_{Hf}V_O)$ defect in HfO_2 may induce nonlinear effects already at lower doping concentrations than Si. Or (ii), the statistic behind the data points of o- and t-phases at 6.25 f.u.% is smaller than for the La_{Hf} defect of the same concentration. The reason for a smaller statistic of $(La_{Hf}V_O)$ is the exclusion of some computations transformed to other phases as discussed in the section "Phase transformation detection during structural relaxation". Nevertheless, the nonlinearity can be considered as not significant.

Künneth et al.[27] have found nonlinear effects of DFT energies of Si_{Hf}-doped HfO_2 at 6.25 f.u.% doping concentration. They only used three different computations (for the three spatial directions) for 6.25 f.u.% doping and chose the lowest energy in the discussion. In Fig. 3c the DFT energies for the 6.25 f.u.% Si_{Hf} defect are the medians of several tens of computations. Similar than in the case of the La_{Hf} defect, this larger statistic of Si_{Hf} results in linear DFT energies for the p-o- and t-phases with increasing doping concentration. Surprisingly, only the t-phase reacts on the increasing amount of Si_{Hf} defects and the crossing of the m- and t-lines can be extrapolated at 8 f.u.%. At this concentration the t-phase becomes the phase of the lowest energy, giving an

explanation for the experimental observation of Si-doped HfO_2 crystallizing in t-phase.[55]

Figure 3d depicts the medians of the DFT energies of Si_{Hf}–La_{Hf}-doped HfO_2. The medians show the linear dependency of the energy evolution with the doping concentration of all phases, except for the p-o-phase. The argument of an insufficient statistics cannot explain this nonlinearity because the size of the statistic for Si_{Hf}–La_{Hf} mixture is the same as for the Si_{Hf} or La_{Hf} sets at equal concentrations. However, because this is the first defect substituting two Hf discussed, Si_{Hf} and La_{Hf} can interact with each other resulting in the steeper change of the total energy of the p-o-phase from 6.25 to 12.5 f.u.% Si_{Hf} La_{Hf}.

Yet another interesting question is why do the 3.125 f.u.% energies of the La_{Hf} and Si_{Hf} defects lie on the line with another data points in the concentration series. For pure HfO_2, there is only one possible structure for each crystal phase. The 6.25 and 12.5 f.u.% data points are backed by statistics of several hundred defect arrangements. On the contrary, the 3.125 f.u.% data points are also represented by a single structure for each phase. Though it is possible to generate statistics in a similar way as is done for higher concentrations. For this, two substitutional defects in a 192-atomic supercell need to be considered. Nevertheless, it seems that this huge number of structures can be represented by only one structure with one substitutional defect in a 96-atomic supercell. The reason for that is that this defect creates not only a homogeneously doped HfO_2 matrix, given the periodic boundary conditions, but this homogeneity is also almost isotropic, because
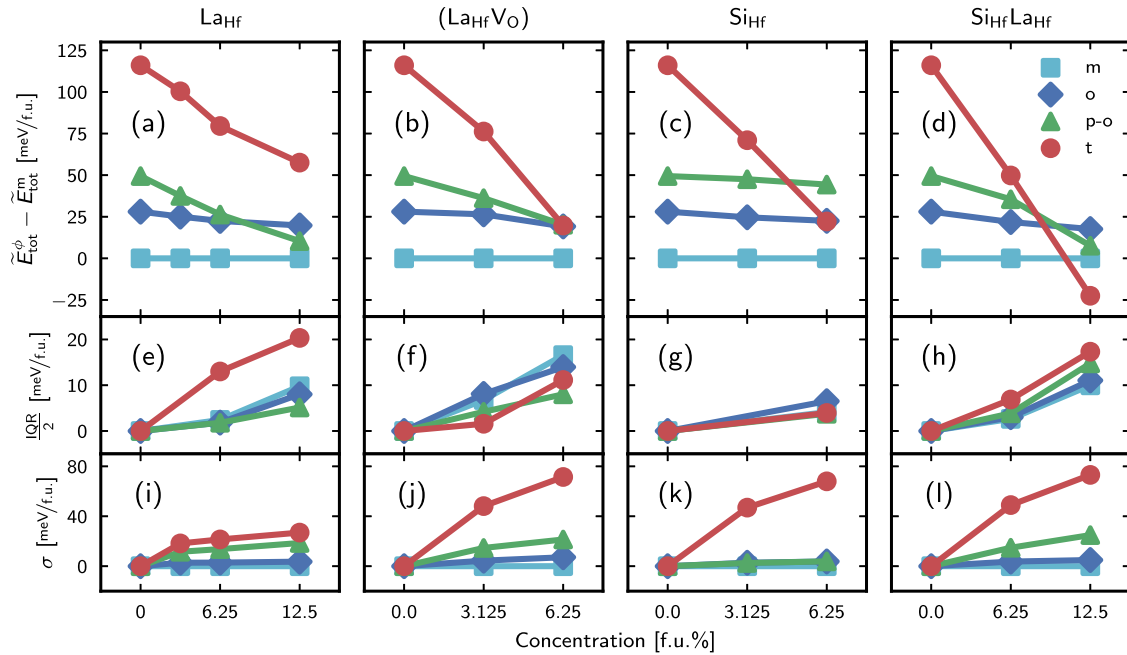
Fig. 3 Total energies against the defect concentration plots for **a** La_{Hf}, **b** $(La_{Hf}V_O)$, **c** Si_{Hf}, and **d** $Si_{Hf}La_{Hf}$ defects in HfO_2. All the points are extracted from Fig. 2 for a better representation of the linear dependencies. The points for the pure HfO_2 and 3.125 f.u.% La_{Hf} and Si_{Hf} defect concentration are single data points. All other points in the plots are the medians of the corresponding distributions. The second row of plots **e–h** shows half the interquartile range IQR(E)/2, as a measure of energy variations caused by dopant interaction, versus defect concentration for the four defects. The third row of plots **i–l** shows $\sigma(\overline{E})$, caused by dopant concentration, versus defect concentration for the four defects
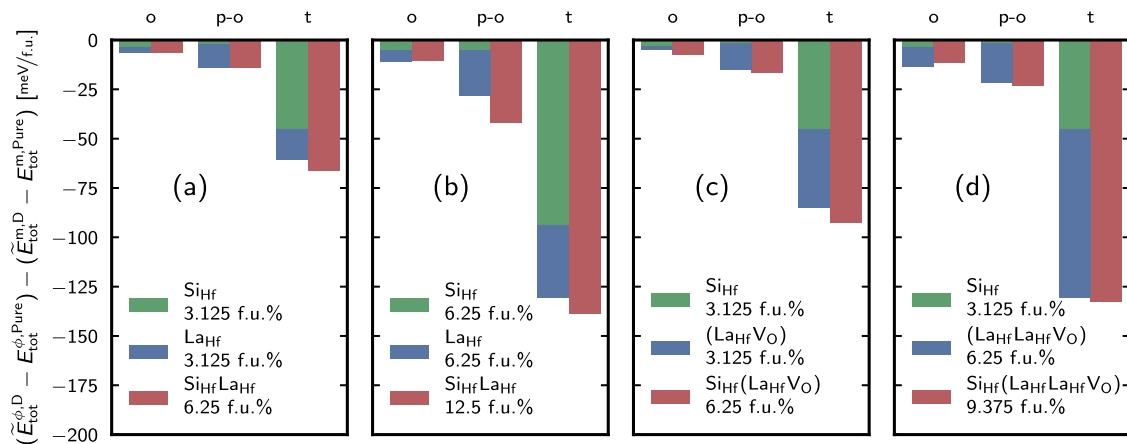

Fig. 4 The effect of the defects on the crystal phases for **a**, **b** $Si_{Hf}La_{Hf}$, **c** $Si_{Hf}(La_{Hf}V_O)$, and **d** $Si_{Hf}(La_{Hf}La_{Hf}V_O)$ mixtures and their constituents in HfO_2. Bars represent the change of the total energies of the o-, p-o-, and t- phases due to the defect, given by $(\tilde{E}_{tot}^{\phi,D} - E_{tot}^{\phi,Pure})$, with respect to the m-phase, the $(\tilde{E}_{tot}^{m,D} - E_{tot}^{m,Pure})$ part. The red bars depict the effect of the mixtures and the green and blue bars depict the effect of their constituents. The bars are drawn using the medians of the statistics

all three lattice constants of the 96-atomic supercell of any HfO_2 phase are approximately 10 Å long. So each defect has six defects next to it in a distance of 10 Å. 6.25 f.u.% doped structure can also be created putting one defect in a 48-atomic supercell. This also leads to homogeneous doping, but one lattice constant of the supercell is twice as short as the two others. This results in a strong anisotropy of the defect density. This anisotropy is canceled out when the statistics of several hundreds of locally inhomogeneous defect arrangements are considered.

Figure 3d shows that the crystal phase total energies go linearly with defect concentration to a certain extent also for a mixture of two defects. An interesting question is whether the effects of single defects in the mixture on the total energy can be

superimposed. The effect of a defect on the total energy of a crystal phase is defined by the energy difference of the doped HfO_2 structure and the undoped HfO_2 in this phase. For instance, the effect of 3.125 f.u.% Si_{Hf} doping on the t-phase is 71 meV/f.u. – 116 meV/f.u. = −45 meV/f.u. (middle and left red points in Fig. 3c). Similarly, the effect of 3.125 f.u.% La_{Hf} on the t-phase is −16 meV/f. u. (see Fig. 3a). These two numbers are represented as green and blue bars in Fig. 4a. The sum of the two effects is approximately equal to the effect of 6.25 f.u.% Si_{Hf}−La_{Hf}-doped t-phase, which is equal to −66 meV/f.u. (see Fig. 3d) and represented by the red bar in Fig. 4a. The same holds for the o- and p-o-phases. The m-phase is generally not depicted in Fig. 4, because each *set* is referenced

to its m-phase and the effect of any defect on the total energy of the m-phase is always zero.

Figure 4b supports the argument for the nonlinearity of the p-o-line in Fig. 3d. For the o- and t-phases, the green and blue bars of the Si_{Hf} and La_{Hf} defects approximately sum up to the red bar of the $Si_{Hf}-La_{Hf}$ mixture. Thus, the mixture constituents do not interact with each other in these crystal phases. On the contrary, the red p-o-phase bar of the mixture is 50% higher than the sum of the green and blue bars of the constituents. Consequently, the $Si_{Hf}-La_{Hf}$ defects start to interact at 12.5 f.u.% and exert a stronger effect on the stability of the p-o-phase. Both Figs. 3d and 4b visualize it from two different approaches.

The effects superposition can also be shown for more complicated defects. Figure 4c shows that the effect on the crystal phase total energies of freely distributed Si_{Hf} and $(La_{Hf}V_O)$ defects with the total concentration of 6.25 f.u.% is given by the sum of the contribution of the single defects with 3.125 f.u.% concentration each. Figure 4d reveals the same for freely distributed $Si_{Hf}-(La_{Hf}La_{Hf}V_O)$ defects pair at 9.375 f.u.%.

This finding allows the assumption that the effect of a mixture of two defects on the phase total energies can be approximated by the sum of the effects of its constituents. This again can be formulated as the appearance of Vegard's rule.

A crucial point in the computation of defects in periodic DFT calculations is the interaction of the incorporated defects, which differs for their concentration and distribution. For sufficient dilute dopant concentrations, no interaction and energetic influence are expected. Differently, for denser concentrations and possible enforced defect distributions (i.e. in the case of ALD manufactured films), in which defects in denser areas interact while defects in diluted areas do not. Generally speaking, the interaction increases with the point defect density, which is determined by the manufacturing process. Attempting to quantify these interactions, formation energies E_f of the single La and Si defect in HfO_2 in the t-phase are computed for three different supercell sizes and illustrated in Fig. 5. The larger the supercell, the greater the distance to the next dopant. The results evidence that the formation energy saturates at a $2 \times 2 \times 2$ supercell meaning that defects at distances larger than 1 nm do not interact, which reflects a sufficiently dilute concentration. In the distance range of 0.5–1 nm, the defects do interact, which is precisely the distance range of two defects in the 48- or 96-atomic supercell computed in this study. The natural length scale of our coarse-grained model for the interaction energy variation turns out to be $\xi = 1$ nm. Since the energies of all positional arrangements of dopants in the 48- and 96-atomic unit cells in Table 1 are computed, the distance-dependent interactions of the defects are already included in the statistic as error bars shown in Fig. 2. Therefore, we can argue that the IQRs in Fig. 2, which are illustrated separately in Fig. 3e–h, are caused by the dopant−dopant interactions and increase with increasing doping concentration. Note that the IQRs in Fig. 2 do not contain a statistical contribution $\sigma(\overline{E})$. These arise from a statistical variation $\sigma(\overline{c})$ of the averaged concentration and

depend on the sensitivity as $\sigma(\overline{E}) = \frac{\partial \overline{E}}{\partial c}\sigma(\overline{c})$. Figure 3i–l contains these values. The concentration dependence has the same interaction length ξ as the individual dopants because a concentration gradient is modeled with a similar supercell with inserted dopant atoms.

In the introduction, three different manufacturing processes were discussed, revealing three different dopant distributions, see also Fig. 1. Since we have shown in the previous paragraphs that the energy evolution with increasing doping concentration is linear and an additional energy variation resulting from a dopant −dopant distance-dependent interaction must be included, we can decide which energy must be considered for specific manufacturing processes. In the case of the ceramics process, in which a large thermal budget is available during the crystallization process, the structure is expected to be in or close to the thermodynamic equilibrium (lowest-energy structures). Mostly structures with low energy are realized and the lower whiskers in Fig. 2 are essential for the energy and phase stability. Moreover, the energy variations in the film from dopant−dopant interactions are expected to be very shallow.

In the case of CSD-manufactured films, the dopants can be considered to be homogeneously distributed after processing because of the liquid precursor and the low thermal budget during the anneal. Therefore, all positional arrangements would be randomly realized in the film. Overall, the energy and the phase stability of the CSD-manufactured film would be determined by the energy median, as shown in Fig. 3a–d. The energy variations in the film, possibly causing nanoregions, are a superposition from concentration variation as shown in Fig. 3i–l and dopant interaction in Fig. 3e–h. The dopant distribution of ALD-manufactured films is more complex. Doping on the level of 6.25 f.u.% is realized by a single deposition cycle of an Si precursor followed by about 15 deposition cycles of Hf. Since a single layer realizes only a fraction of a monolayer, the Si concentration is modeled as a 1-nm-thick region of 12.5 f.u.% Si. It is experimentally shown[36,37] that metal movements are suppressed by the low thermal budget during the anneal. The dopant distribution orthogonal to the surface of the film would lead to a wavy energy evolution superimposed by energy variations. But the energy variations are much stronger in the dopant layers compared to CSD due to the concentration dependence of the variation shown in Fig. 3e–l, increasing the possibility for nanoregions.

Figure 1 shows the nanoscaled energy variations in CSD and ALD Si-doped HfO_2 films in the p-o- and t-phases due to the local doping distribution inhomogeneities in a coarse-grained representation in $1 \times 1 \times 1$ nm^3 units. For the CSD film, a constant average concentration of 6.25 f.u.% is chosen that corresponds to two Si atoms per discretization unit. For each unit the number of Si atoms is randomly chosen in accordance to the Poisson distribution resulting in the variance of the local concentration $\sigma(\overline{c})$ and hence the energy $\sigma(\overline{E})$ (Fig. 3k). The additional energy variation stemming from the defect−defect interaction is drawn from an assumed normal distribution with the standard deviation equal to IQR(E)/2 (Fig. 3g). For the ALD films, the layers of 1 nm thickness are chosen. Within each layer, the doping concentration is constant on average, while along the growth direction it alternates between 0 and 12.5 f.u.%. In the undoped layers, both types of the energy variation are equal to zero. For the doped layers, the variations are calculated in the same manner as for the CSD film with appropriate $\sigma(\overline{E})$ and IQR(E)/2. Finally, both energy variations are added to the energy profile originating from the average doping concentration, which is constant for the CSD and alternating for the ALD film. Owing to the independent total energy of the p-o-phase on the defect concentration, the energy variation $\sigma(\overline{E})$ is small in comparison to IQR(E)/2 (Fig. 3g, k). Hence, the defect−defect interaction is the main contributor to the energy variance of the p-o-phase for both the CSD and ALD Si-doped HfO_2 films. On contrary, for the t-phase the energy
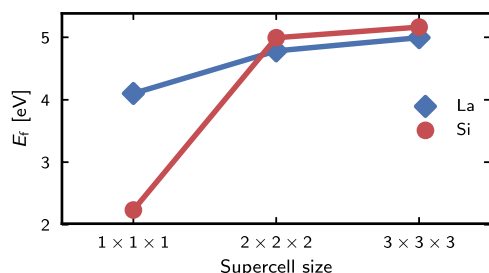
Fig. 5 Formation energies of La and Si defects in HfO_2 t-phase in dependence on the supercell size, according to Eq. (1). $2 \times 2 \times 2$ corresponds to $\xi = 1$ nm

variance is mainly based on the local variations of the defect concentration.

For instance, the Curie temperature is broadened during the transformation from the polar to the nonpolar phase in experimental measurements,[41,42] possibly owing to the nanos-caled energy domains. Due to the high crystal symmetry of the t-phase its Helmholtz free energy is decreasing faster with the increasing temperature if compared to the p-o-phase. Therefore, the rising temperature results in the downwards shift of the energy landscape of the t-phase with respect to the p-o-phase, which leads to the gradual switching of the domains from the p-o-phase to the t-phase.

The range of interaction of La or/and Si dopants in HfO$_2$, relevant for the stability of the ferroelectric p-o-phase relative to the t-phase, has been calculated as $\xi = 1$ nm. High-throughput calculations with 1 nm-sized supercells for all relevant crystal phases produce low energy structures, median energy values, and unexpectedly large energy variation IQR(E), caused by the dopant interaction. The current approach is an improvement to our previous studies because it now considers big statistics and allows to relate the data to different production processes. As there is additionally a statistical deviation $\sigma(\bar{E})$ in any control volume, the detection of IQR(E) seems only possible in a coarse-grained approach with discretization units of size ξ. When evaluating the data, the dependence of median energies on the average concentration turns out to be almost linear, even in the mixture of defects, resembling Vegard's rule. The relevance of the energy variation is considered with regard to the competition between the dielectric t-phase and ferroelectric p-o-phase. As nanoregions in this material have been suggested and nanolaminate effects have been identified, the theoretical results obtained here are an important step to fundamentally substantiate the experimental findings. The formation of nanoregions with different phases requires interphase boundaries with additional energy contribu-tions. The related and experimentally observed effect of the Curie temperature broadening can be investigated utilizing the Monte Carlo method. The condition for the appearance of the interphase boundaries and diffuse phase transition with increasing tempera-ture are the topics of further research.

METHODS

Geometries setup for the calculations
The primitive unit cells for the m-, o-, p-o-, and t-crystal phases consist of 12, 24, 12, and 6 atoms, respectively. For convenience, a 12-atomic cell for the t-phase can be constructed through a coordinate transformation. The c-phase is omitted, because it always disintegrates into the t-phase during the ionic force relaxation. It is also expected, because the c-phase is stabilized dynamically at high temperatures and has disadvantageous energy at 0 K, a condition of DFT calculations. In this study, supercells consisting of 48 and 96 atoms are considered. For the m-, p-o- and t-phases a $2 \times 2 \times 2$ supercell and for the o-phase a $1 \times 2 \times 2$ supercell sum up to 96 atoms. There are, though, three possible orientations for a 48-atomic supercell for m-, p-o-, and t- phases: $1 \times 2 \times 2$, $2 \times 1 \times 2$ or $2 \times 2 \times 1$. For the o-phase only two orientations $1 \times 1 \times 2$ or $1 \times 2 \times 1$ are possible due to the double amount of atoms in the primitive cell.

The number of possible arrangements of two substitutional dopants on the metal sites in, for instance, a 96-atomic supercell with 32 Hf atoms is $32 \times 31 = 992$. Due to the symmetry, a lot of these arrangements are equal. Hence, not for all possible arrangements, a DFT calculation needs to be performed. In a supercell of any size metal sites in all here considered crystal phases are equivalent by symmetry. It does not play any role on which metal site the first substitutional dopant is placed. The presence of this dopant in the supercell though reduces the spatial symmetry, so the remaining 31 metal sites for the second substitutional dopant are in general not equivalent. For this reason, at most, 31 DFT calculations are needed for covering the whole space of arrangements of two substitu-tional dopants on the metal sites in a 96-atomic supercell. For the t-phase this number is further reduced due to the high symmetry of the crystal phase compared to the other three phases. The number of needed

computations is also reduced if the two substitutional dopants are of the same kind, and so indistinguishable.

Similar arguments hold for placing an oxygen vacancy in supercells during the structures set up for calculations. In m-, o- and p-o-phases there are only two by symmetry nonequivalent oxygen sites, regardless of the supercell size. In the t-phase all oxygen sites are equal by symmetry.

Freely distributed La$_{Hf}$−La$_{Hf}$−V$_O$ defects in, for instance, a 96-atomic p-o-supercell require almost 2000 calculations, even after reduction of arrangement space due to the symmetry. Further reduction can be made assuming that a tight complex (La$_{Hf}$La$_{Hf}$V$_O$) is build due to the electrostatic attraction. Any oxygen or hafnium site in any phase has four hafnium or eight oxygen next-neighbor sites, respectively.

In comparison to 96-atomic supercell, a 48-atomic supercell can be differently oriented. For instance, $16 \times 15 \times 3 = 720$ arrangements of two dopants of a different kind in a 48-atomic p-o-supercell with 16 metal sites are possible. The number of needed calculations can be reduced, though, in the same manner as discussed above.

Defect formation energy
For Fig. 5, the defect formation energies in HfO$_2$ supercells of different size are calculated. The structures for the three different supercell sizes are prepared in a special way and only single-shot calculations of the total energies without the ionic relaxation are performed. The setup procedure for the structure is as follows. First, a 12-atomic cell in t-phase with one Hf substituted by a defect is relaxed, which changes the lattice constants and the oxygen atoms around the defect form a characteristic tetrahedron arrangement. While keeping the reduced coordinates of the relaxed doped structure intact, the lattice constants are set to the values of the pure HfO$_2$ t-phase cell in order to build pre-relaxed 48- and 96-atomic doped cells. Second, an HfO$_2$ supercell in the t-phase of needed size is constructed and one 12-atomic section is substituted by the relaxed and scaled cell with the defect prepared in the first step. The result is a doped HfO$_2$ supercell, structurally mostly equal to the pure t-phase with adjusted crystal structure in the vicinity of the defect. The formation energy of a substitutional defect in the HfO$_2$ matrix is the energy for replacing one Hf with the doping atom. Additionally, the chemical potentials of Hf and the dopant are also needed. The chemical potential of Hf is the energy for incorporating the removed Hf into some reference structure like metallic hafnium. On the contrary, the chemical potential of the dopant gives the energy for creation of one free atom from some reference structure. Hence, the formation energy of a defect is given as follows:

$$E_f^D = E_{tot}^D - E_{tot}^{Pure} - \mu^D + \mu^{Hf}, \qquad (1)$$

where μ^D and μ^{Hf} are the chemical potentials of La, Si and Hf atoms, which are calculated from pure lanthanum, silicon and hafnium metals, respectively.

Phase transformation detection during structural relaxation
In total, more than 2500 DFT calculations are needed for this study. For each doped structure, a structural relaxation must be performed, which leads to changes of the supercell and the positions of all atoms compared to the pure HfO$_2$ host. None of the structures can retain its initial space group symmetry, not only due to the introduced doping defects but also due to the structural deformation after the relaxation. Only by means of certain characteristics of the relaxed structures, like lattice constants, their ratios, lattice angles, positions of the oxygen atoms with respect to the metal atoms, they can be related to a certain crystal phase. Furthermore, a doped structure can even transform from its initial phase into another one during the relaxation of ionic forces. Such transformations must be filtered out for further evaluation of the calculations.

It is rather a rare case that a structure transforms into another crystal phase. Therefore, it is sufficient enough to compare calculations with each other within a single set to filter out the cases of the phase transformation.

The m- and o-phases have greater supercell volume than the p-o- and t-phases. Additionally, the m-phase has one sharp angle and the o-phase has only right angles. The relaxed structures comparing with each other can be unambiguously classified into the m- or o-phase by these two characteristics.

The distinction between the p-o- and t-phases is more complicated. We have found empirically that the Hirshfeld charge analysis,[56] which can be performed by FHI-AIMS, gives a good criterion for distinguishing the p-o-phase from the t-phase. For the m-, o-, and t-phases of the pure HfO$_2$, the vector sum of the electron dipole moments is a zero-vector. For the

p-o-phase this is a vector of 0.01856 eÅ/f.u. length, which is chosen to be a reference. The doped m-, o-, and t-supercells have a finite dipole moments sum due to the presence of the defect, of course. Nevertheless, these phases can still be clearly separated from the doped p-o-supercells.

All the described procedures can be performed in an automated manner, which not only saves evaluation time but also excludes the subjective nature of the human eye if the classification of the relaxed structures were performed by hand.

DFT calculations

All DFT calculations in this paper were performed with the all-electron code FHI-AIMS[57] using the local density approximation[58] (LDA). FHI-AIMS uses tabulated numeric, atom-centered orbitals as the basis set. The simulations were conducted using the tight settings of basis set additionally enabling the complete first and second tiers for the atom species. The convergence criteria were set to 1×10^{-4} and 1×10^{-2} eV/Å for electronic and ionic forces, respectively. FHI-AIMS utilizes the Monkhorst-Pack[59] grid for the k-point grid definition. For supercells consisting of 96 atoms (95 with a vacancy), a $2 \times 2 \times 2$ grid was chosen. For supercells consisting of 48 atoms (47 with a vacancy) $4 \times 2 \times 2$, $2 \times 4 \times 2$ or $2 \times 2 \times 4$ grid was chosen depending on the orientation of the supercell, as discussed in the section "Geometries setup for the calculations". All these settings were found to be sufficient in a convergence study.

DATA AVAILABILITY

The datasets for the study are available from the corresponding authors upon request.

AUTHOR CONTRIBUTIONS

M.F. and A.K. designed the study and the methodology. M.F. carried out the calculations, evaluated the results and produced the figures. All authors analyzed the findings and wrote the manuscript. M.F. is guarantor of the presented study.

ADDITIONAL INFORMATION

Supplementary information accompanies the paper on the npj Computational Materials website (https://doi.org/10.1038/s41524-018-0133-4).

Competing interests: The authors declare no competing interests.

Publisher's note: Springer Nature remains neutral with regard to jurisdictional claims in published maps and institutional affiliations.

REFERENCES

1. Keyes, R. W. Physical limits of silicon transistors and circuits. *Rep. Progress. Phys.* **68**, 2701–2746 (2005).
2. Böscke, T. S., Müller, J., Bräuhaus, D., Schröder, U. & Böttger, U. Ferroelectricity in hafnium oxide thin films. *Appl. Phys. Lett.* **99**, 102903 (2011).
3. Toriumi, A. (Invited) High-k, higher-k and ferroelectric HfO₂. *ECS Trans.* **80**, 29–40 (2017).
4. Park, M. H. et al. Ferroelectricity and antiferroelectricity of doped thin HfO₂-based films. *Adv. Mater.* **27**, 1811–1831 (2015).
5. Ahnert, S. E., Grant, W. P. & Pickard, C. J. Revealing and exploiting hierarchical material structure through complex atomic networks. *npj Comput. Mater.* **3**, 35 (2017).
6. Kaski, K., Binder, K. & Gunton, J. D. A study of a coarse-grained free energy functional for the three-dimensional Ising model. *J. Phys. A: Math. General.* **16**, L623–L627 (1983).
7. Cross, L. E. Relaxor ferroelectrics. *Ferroelectrics* **76**, 241–267 (1987).
8. Krogstad, M. J. et al. The relation of local order to material properties in relaxor ferroelectrics. *Nat. Mater.* **17**, 718–724 (2018).
9. Xu, G., Wen, J., Stock, C. & Gehring, P. M. Phase instability induced by polar nanoregions in a relaxor ferroelectric system. *Nat. Mater.* **7**, 562–566 (2008).
10. Seyf, H. R. et al. Rethinking phonons: the issue of disorder. *npj Comput. Mater.* **3**, 49 (2017).
11. Bokov, A. A. & Ye, Z. G. Recent progress in relaxor ferroelectrics with perovskite structure. In Lang, S. B. & Chan, H. L. W. (eds.) *Frontiers of Ferroelectricity: A Special Issue of the Journal of Materials Science* 31–52 (Springer US, Boston, MA, 2007).
12. Groszewicz, P. B. et al. Reconciling local structure disorder and the relaxor state in (Bi₁/₂Na₁/₂)TiO₃-BaTiO₃. *Sci. Rep.* **6**, 31739 (2016).
13. Azadmanjiri, J. et al. A review on hybrid nanolaminate materials synthesized by deposition techniques for energy storage applications. *J. Mater. Chem. A* **2**, 3695–3708 (2014).
14. Lee, G., Fuentes-Fernandez, E. M. A., Lian, G., Katiyar, R. S. & Auciello, O. Hetero-epitaxial BiFeO₃/SrTiO₃ nanolaminates with higher piezoresponse performance over stoichiometric BiFeO₃ films. *Appl. Phys. Lett.* **106**, 022905 (2015).
15. Weeks, S. L., Pal, A., Narasimhan, V. K., Littau, K. A. & Chiang, T. Engineering of ferroelectric HfO₂–ZrO₂ nanolaminates. *ACS Appl. Mater. Interfaces* **9**, 13440–13447 (2017).
16. Shvartsman, V., Dkhil, B. & Kholkin, A. Mesoscale domains and nature of the relaxor state by piezoresponse force microscopy. *Annu. Rev. Mater. Res.* **43**, 423–449 (2013).
17. Li, F. et al. The origin of ultrahigh piezoelectricity in relaxor-ferroelectric solid solution crystals. *Nat. Commun.* **7**, 13807 (2016).
18. Müller, J. et al. Ferroelectricity in simple binary ZrO₂ and HfO₂. *Nano Lett.* **12**, 4318–4323 (2012).
19. Starschich, S., Griesche, D., Schneller, T. & Böttger, U. Chemical solution deposition of ferroelectric hafnium oxide for future lead free ferroelectric devices. *ECS J. Solid State Sci. Technol.* **4**, P419–P423 (2015).
20. Starschich, S. & Boettger, U. An extensive study of the influence of dopants on the ferroelectric properties of HfO₂. *J. Mater. Chem. C* **5**, 333–338 (2017).
21. Shimizu, T. et al. The demonstration of significant ferroelectricity in epitaxial Y-doped HfO₂ film. *Sci. Rep.* **6**, 32931 (2016).
22. Zhu, H., Tang, C., Fonseca, L. R. C. & Ramprasad, R. Recent progress in ab initio simulations of hafnia-based gate stacks. *J. Mater. Sci.* **47**, 7399–7416 (2012).
23. Barabash, S. V. Prediction of new metastable HfO₂ phases: toward understanding ferro- and antiferroelectric films. *J. Comput. Electron.* **16**, 1227–1235 (2017).
24. Xu, L. et al. Kinetic pathway of the ferroelectric phase formation in doped HfO₂ films. *J. Appl. Phys.* **122**, 124104 (2017).
25. Materlik, R., Künneth, C., Mikolajick, T. & Kersch, A. The impact of charge compensated and uncompensated strontium defects on the stabilization of the ferroelectric phase in HfO₂. *Appl. Phys. Lett.* **111**, 082902 (2017).
26. Materlik, R., Künneth, C., Falkowski, M., Mikolajick, T. & Kersch, A. Al-, Y-, and La-doping effects favoring intrinsic and field induced ferroelectricity in HfO₂: a first principles study. *J. Appl. Phys.* **123**, 164101 (2018).
27. Künneth, C., Materlik, R., Falkowski, M. & Kersch, A. Impact of four-valent doping on the crystallographic phase formation for ferroelectric HfO₂ from first-principles: implications for ferroelectric memory and energy-related applications. *ACS Appl. Nano Mater.* **1**, 254–264 (2018).
28. Robertson, J. & Wallace, R. M. High-K materials and metal gates for CMOS applications. *Mater. Sci. Eng. R: Rep.* **88**, 1–41 (2015).
29. Mueller, W. et al. Challenges for the DRAM cell scaling to 40 nm. In *IEEE International-Electron Devices Meeting, 2005*. IEDM Technical Digest, Vol. 1, 336 −339 (IEEE, 2005).
30. Parkes, M. A. et al. The atomistic structure of yttria stabilised zirconia at 6.7 mol%: An ab initio study. *Phys. Chem. Chem. Phys.* **18**, 31277–31285 (2016).
31. Sang, X., Grimley, E. D., Schenk, T., Schroeder, U. & Lebeau, J. M. On the structural origins of ferroelectricity in HfO₂ thin films. *Appl. Phys. Lett.* **106**, 162905 (2015).
32. Mikolajick, T., Slesazeck, S., Park, M. H. & Schroeder, U. Ferroelectric hafnium oxide for ferroelectric random-access memories and ferroelectric field-effect transistors. *MRS Bull.* **43**, 340–346 (2018).
33. Predith, A., Ceder, G., Wolverton, C., Persson, K. & Mueller, T. Ab initio prediction of ordered ground-state structures in ZrO₂-Y₂O₃. *Phys. Rev. B—Condens. Matter Mater. Phys.* **77**, 144104 (2008).
34. Stolichnov, I. et al. Genuinely ferroelectric sub-1-volt-switchable nanodomains in Hf$_x$Zr$_{(1−x)}$O₂ ultrathin capacitors. *ACS Appl. Mater. Interfaces.* **10**, 30514–30521 (2018).
35. Mittmann, T. et al. Optimizing process conditions for improved Hf₁−ₓZrₓO₂ ferroelectric capacitor performance. *Microelectron. Eng.* **178**, 48–51 (2017).
36. Lomenzo, P. D. et al. The effects of layering in ferroelectric Si-doped HfO₂ thin films. *Appl. Phys. Lett.* **105**, 072906 (2014).

37. Richter, C. et al. Si doped hafnium oxide—a "fragile" ferroelectric system. *Adv. Electron. Mater.* **3**, 1700131 (2017).

38. Starschich, S. & Böttger, U. Doped ZrO$_2$ for future lead free piezoelectric devices. *J. Appl. Phys.* **123**, 044101 (2018).

39. Pešić, M. et al. Physical mechanisms behind the field-cycling behavior of HfO$_2$-based ferroelectric capacitors. *Adv. Funct. Mater.* **26**, 4601–4612 (2016).

40. Pešić, M. et al. A computational study of hafnia-based ferroelectric memories: from ab initio via physical modeling to circuit models of ferroelectric device. *J. Comput. Electron.* **16**, 1236–1256 (2017).

41. Hoffmann, M. et al. Ferroelectric phase transitions in nanoscale HfO$_2$ films enable giant pyroelectric energy conversion and highly efficient supercapacitors. *Nano Energy* **18**, 154–164 (2015).

42. Park, M. H. et al. Origin of temperature-dependent ferroelectricity in Si-doped HfO$_2$. *Adv. Electron. Mater.* **4**, 1700489 (2018).

43. Lee, C.-K., Cho, E., Lee, H.-S., Hwang, C. S. & Han, S. First-principles study on doping and phase stability of HfO$_2$. *Phys. Rev. B* **78**, 012102 (2008).

44. Fischer, D. & Kersch, A. Stabilization of the high-k tetragonal phase in HfO$_2$: the influence of dopants and temperature from ab initio simulations. *J. Appl. Phys.* **104**, 084104 (2008).

45. Batra, R., Huan, T. D., Rossetti, G. A. & Ramprasad, R. Dopants promoting ferroelectricity in hafnia: insights from a comprehensive chemical space exploration. *Chem. Mater.* **29**, 9102–9109 (2017).

46. Fischer, D. & Kersch, A. The effect of dopants on the dielectric constant of HfO$_2$ and ZrO$_2$ from first principles. *Appl. Phys. Lett.* **92**, 012908 (2008).

47. Parkes, M. A. et al. Chemical descriptors of yttria-stabilized zirconia at low defect concentration: An ab initio study. *J. Phys. Chem. A* **119**, 6412–6420 (2015).

48. Curtarolo, S. et al. The high-throughput highway to computational materials design. *Nat. Mater.* **12**, 191–201 (2013).

49. Schroeder, U. et al. Lanthanum-doped hafnium oxide: a robust ferroelectric material. *Inorg. Chem.* **57**, 2752–2765 (2018).

50. Buragohain, P. et al. Nanoscopic studies of domain structure dynamics in ferroelectric La:HfO$_2$ capacitors. *Appl. Phys. Lett.* **112**, 222901 (2018).

51. Grimley, E. D., Schenk, T., Mikolajick, T., Schroeder, U. & LeBeau, J. M. Atomic structure of domain and interphase boundaries in ferroelectric HfO$_2$. *Adv. Mater. Interfaces* **5**, 1701258 (2018).

52. Künneth, C., Materlik, R. & Kersch, A. Modeling ferroelectric film properties and size effects from tetragonal interlayer in Hf$_{1-x}$Zr$_x$O$_2$ grains. *J. Appl. Phys.* **121**, 205304 (2017).

53. Materlik, R., Künneth, C. & Kersch, A. The origin of ferroelectricity in Hf$_{1-x}$Zr$_x$O$_2$: a computational investigation and a surface energy model. *J. Appl. Phys.* **117**, 134109 (2015).

54. Batra, R., Huan, T. D., Jones, J. L., Rossetti, G. & Ramprasad, R. Factors favoring ferroelectricity in hafnia: a first-principles computational study. *J. Phys. Chem. C* **121**, 4139–4145 (2017).

55. Böscke, T. S. et al. Stabilization of higher-κ tetragonal HfO$_2$ by SiO$_2$ admixture enabling thermally stable metal-insulator-metal capacitors. *Appl. Phys. Lett.* **91**, 072902 (2007).

56. Hirshfeld, F. L. Bonded-atom fragments for describing molecular charge densities. *Theor. Chim. Acta* **44**, 129–138 (1977).

57. Blum, V. et al. Ab initio molecular simulations with numeric atom-centered orbitals. *Comput. Phys. Commun.* **180**, 2175–2196 (2009).

58. Perdew, J. P. & Wang, Y. Accurate and simple analytic representation of the electron-gas correlation energy. *Phys. Rev. B* **45**, 13244–13249 (1992).

59. Monkhorst, H. J. & Pack, J. D. Special points for Brillouin-zone integrations. *Phys. Rev. B* **13**, 5188–5192 (1976).